Counter-Rotating Propeller Analysis Using a Frequency Domain Panel Method

Jinsoo Cho* and Marc H. Williams†
Purdue University, West Lafayette, Indiana 47907

The unsteady aerodynamic coupling between the front and rear rotors in a counter-rotating propeller system is analyzed using a frequency-domain panel method based on linear compressible aerodynamic theory. The periodic loads are decomposed into harmonics, and the harmonic amplitudes are found iteratively. Each stage of the iteration involves the solution of an isolated propeller problem, the interaction being done through the Fourier transform of the induced velocity field. The method was validated by comparing mean performance parameters with measured data and by comparing the predicted velocity field with detailed laser Doppler velocimeter measurements. Comparisons have also been made between the fluctuating loads predicted by the present method and a time-domain panel method.

Introduction

IT is the objective of this paper to present a numerical method for the prediction of the unsteady aerodynamic forces which arise from the interaction between the front and rear rotor blades of a counter-rotating propeller system. Results for mean and fluctuating loads and for the induced velocity field will be compared to experimental data and alternative calculations. The scheme is intended to provide a practical method for calculating the unsteady aerodynamic forces that are needed for the aeroelastic analysis of counter-rotating propeller (CRP) systems.

Of the many theoretical and experimental papers related to propellers, we will mention only those that directly apply to the present work. In 1942, Biermann and Hartman[1] conducted wind-tunnel tests of single and counter-rotating propellers with 4 and 6 (total) number of blades. The front and rear rotors were powered separately so that the power split between the two is known. Their measured performance curves have been used to validate our numerical results. Harrison and Sullivan[2,3] measured the unsteady flowfield around a CRP system using Laser Doppler Velocimetery (LDV). These data provide a direct experimental check on the validity of the present unsteady aerodynamic model.

On the analytical side, Lesieutre and Sullivan[4,5] analyzed a CRP system by applying a stripwise Sears correction to the quasisteady incompressible solution obtained with a vortex lattice method. Their mean performance results showed good agreement with experiment, but the predicted unsteady load fluctuations are suspect. Chen and Williams[6] solved the fully unsteady, incompressible CRP problem using a time-domain potential panel method. Their mean loads agreed with those and Lesieutre and Sullivan, but their unsteady load fluctuations differed substantially when the reduced frequency was high. Both Lesieutre and Sullivan and Chen and Williams used a rigid wake model and were limited to low Mach numbers.

There are also a number of computational fluid dynamics (CFD) codes available, both at the Euler and Navier-Stokes levels, which can handle rotor-rotor interaction. Such schemes provide, in principle, greater accuracy than is available from the less complete models but at much higher cost.

The present calculation is based on the lifting surface panel method developed by Williams and Hwang[7-9] for the unsteady aerodynamic analysis of single rotation propellers (SRP) for which the blade loading can be represented by a single frequency. The panel method is based on linearized compressible aerodynamics so that the low-speed assumption of Lesieutre and Sullivan and Chen and Williams is not made (though the examples to be presented in this paper are all low speed). However the two dominant aerodynamic nonlinearities, transonic shocks, and wake rollup, are not included in the model. This lifting surface theory has been applied extensively and successfully to the prediction of flutter and forced vibration of single rotation propfans.[9-12]

To extend this method to CRP systems, the loads are represented with multiple harmonics, which interact through their induced velocity fields. The first such extension to relative rotation was given in Ref. 13 in a study of the interaction between a wing and a tractor-mounted propeller. The harmonic balance formulation of the CRP problem given here is general and includes the wing propeller as a special case. The panel method itself is identical to the single rotation case and will not be described in detail.

Methodology

We shall consider the interaction of two rotors, labeled F (front) and R (rear). Each rotor is assumed to be tuned, i.e., to consist of identical equally spaced blades. The number of blades, the revolutions per minute (rpm), and the blade geometry of the two rotors may be different. The coordinates used to define the rotor positions are illustrated in Fig. 1.

The unsteady interaction between the front and rear rotors in a CRP system can be expressed by a pair of linear relations between the instantaneous normal velocity (V) and pressure difference (Δp) on the respective lifting surfaces,

$$V_F = A_{FF} \cdot \Delta p_F + A_{FR} \cdot \Delta p_R$$

$$V_R = A_{RF} \cdot \Delta p_F + A_{RR} \cdot \Delta p_R \qquad (1)$$

The coefficients A are linear integral space/time operators. Given the normal velocities, the solution (for Δp) can clearly be decomposed into the sum of front-rotor-driven ($V_R = 0$) and rear-rotor-driven ($V_F = 0$) parts. In either case, we suppose that the driver V_α is simple harmonic with given fre-

Recieved Sept. 30, 1988; revision received May 15, 1989.

*Graduate Student; currently visiting Assistant Professor, School of Aeronautics and Astronautics. Member AIAA.

†Associate Professor, School of Aeronautics and Astronautics. Member AIAA.

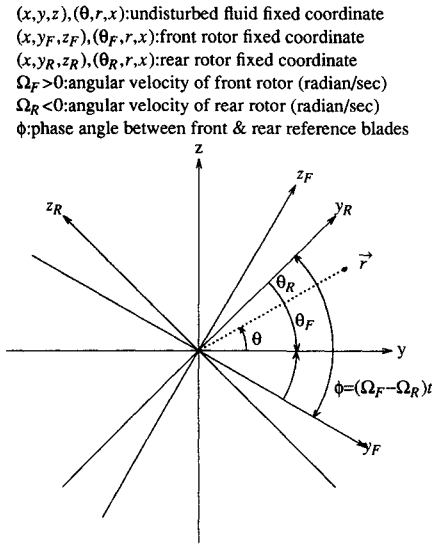

Fig. 1 Counter-rotating propeller coordinate systems.

quency ω_0 and interblade phase index m_0 so that the normal velocity on the jth blade of the driver rotor (α) is (real parts are implied) the following:

$$V_{\alpha_j} = \bar{V}_{\alpha_j} e^{i\omega_0 t - ijm_0\Delta\theta_\alpha} \tag{2}$$

If the frequencies and interblade phases of V_F and V_R are commensurate, the front and rear driven parts interact and should be solved without decomposing into two parts.

By the periodicity of the interaction, the loads on the jth blade of each rotor can be expanded in harmonics as follows:

$$\Delta p_{\alpha_j} = \sum_n P_{\alpha_n} e^{i(\omega_0 + nN_\beta\Omega_0)t - ij(nN_\beta + m_0)\Delta\theta_\alpha}$$

$$\Delta p_{\beta_j} = \sum_n P_{\beta_n} e^{i[\omega_0 + (nN_\alpha - m_0)\Omega_0]t - ij(nN_\alpha - m_0)\Delta\theta_\beta} \tag{3}$$

where the subscripts α and β represent the forcing and receiving rotor, respectively ($\alpha = F$ and $\beta = R$ for front rotor-driven part and $\alpha = R$ and $\beta = F$ for rear rotor-driven part), and

N_γ = number of blades in rotor γ
$\Delta\theta_\gamma = 2\pi/N_\gamma$ = interblade angle of rotor γ
Ω_γ = angular velocity of rotor γ
$\Omega_0 = \Omega_\alpha - \Omega_\beta$

If both rotors are rigid and have the same number of blades (the case examined in this paper) then $\omega_0 = m_0 = 0$. The problem of tractor-mounted, propeller-wing interaction, which was discussed in Ref. 13 is a special case with $\Omega_R = 0$, $N_R = 1$, and $\omega_0 = m_0 = 0$.

The objective is to compute the harmonic load coefficients P_{α_n} and P_{B_n} for given normal velocities V. If we substitute the expansions (3) into Eq. (1) and separate harmonics, we get

$$\bar{A}_{\alpha\alpha}(\omega_0 + nN_\beta\Omega_0,\ nN_\beta + m_0)\cdot P_{\alpha_n} = \bar{V}_{\alpha_n}$$

$$\bar{A}_{\beta\beta}[\omega_0 + (nN_\alpha - m_0)\Omega_0,\ nN_\alpha - m_0)\cdot P_{\beta_n} = \bar{V}_{\beta_n} \tag{4}$$

where $\bar{A}(\omega,k)$ denotes the simple harmonic reference blade operator for frequency ω and interblade phase lag $k\Delta\theta$ (these are the single rotation or isolated rotor operators). The quantities $\bar{V}$ are the complex harmonic amplitudes of the normal velocity on each surface modified by the induced velocity from the other surface. Given $\bar{V}$, Eqs. (4) represent separate simple harmonic problems for the front and rear rotor. Of course the $\bar{V}$ are not given but depend in a complicated way on the loads in all harmonics.

Each load harmonic P_{α_n} on the driving rotor produces a velocity field which is simple harmonic in the driving rotor frame (θ_α),

$$\boldsymbol{u}_{\alpha_n} = \boldsymbol{U}_{\alpha_n}(\theta_\alpha) e^{i(\omega_0 + nN_\beta\Omega_0)t} \tag{5}$$

where the complex amplitude is found by an integral over the reference blade,

$$\boldsymbol{U}_{\alpha_n} = \int\int P_{\alpha_n}(\boldsymbol{x}_0)\boldsymbol{K}_\alpha(\boldsymbol{x},\boldsymbol{x}_0)\ \mathrm{d}A_0 \tag{6}$$

Explicit expressions for the rotor kernel $\boldsymbol{K}_\alpha$ will be found in Ref. 14. Note that the rotor operator $\bar{A}_{\alpha\alpha}$ is simply the normal projection of Eq. (6) on the reference blade.

The velocity field of Eq. (5) can be Fourier expanded in θ_α and transformed to the receiving rotor frame ($\theta_\beta = \theta_\alpha - \Omega_0 t$, see Fig. 1),

$$\boldsymbol{u}_{\alpha_n}(\theta_\beta,t) = e^{i(\omega_0 + nN_\beta\Omega_0)t}\sum_k \left[\boldsymbol{U}_{\alpha_{nk}} e^{iK\theta_\beta}\right] e^{iK\Omega_0 t} \tag{7}$$

where

$$\boldsymbol{U}_{\alpha_{nk}} = \frac{1}{\Delta\theta_\alpha}\int_0^{\Delta\theta_\alpha} \boldsymbol{U}_{\alpha_n}(\theta_\alpha) e^{-iK\theta_\alpha}\mathrm{d}\theta_\alpha$$

$$K = kN_\alpha - nN_\beta - m_0 \tag{8}$$

The velocity field $\boldsymbol{U}_{\alpha_{nk}} e^{iK\theta_\beta}$ corresponds to the receiving rotor frame frequency $\omega_0 + (kN_\alpha - m_0)\Omega_0$ and therefore contributes to the receiving rotor normal velocity $\bar{V}_{\beta_k}$ in Eq. (4) an amount

$$\Delta\bar{V}_{\beta_k} = -\boldsymbol{n}_\beta \cdot \boldsymbol{U}_{\alpha_{nk}} e^{iK\theta_\beta} \tag{9}$$

where $\boldsymbol{n}_\beta$ is the normal to the receiving rotor camber surface.

Similarly, each load harmonic P_{β_n} on the receiving rotor produces a velocity field, which is simple harmonic in that rotor frame (θ_β),

$$\boldsymbol{u}_{\beta_n} = \boldsymbol{U}_{\beta_n}(\theta_\beta) e^{i[\omega_0 + (nN_\alpha - m_0)\Omega_0]t} \tag{10}$$

where the complex amplitude can be found by an integral over the reference blade as in Eq. (6) but with $\alpha \to \beta$. This velocity field, too, can be Fourier expanded in θ_β and transformed to the driving rotor frame, $\theta_\alpha = \theta_\beta + \Omega_0 t$,

$$\boldsymbol{u}_{\beta_n}(\theta_\alpha,t) = e^{i[\omega_0 + (nN_\alpha - m_0)\Omega_0]t}\sum_k \left(\boldsymbol{U}_{\beta_{nk}} e^{iK\theta_\alpha}\right) e^{-iK\Omega_0 t} \tag{11}$$

where $K = kN_\beta - nN_\alpha + m_0$, and the amplitude $\boldsymbol{U}_{\beta_{nk}}$ is computed from Eq. (8) (with $\alpha \to \beta$). The velocity field $\boldsymbol{U}_{\beta_{nk}} e^{iK\theta_\alpha}$ corresponds to the driving rotor frame frequency $\omega_0 + kN_\beta\Omega_0$ and therefore contributes to the driving rotor normal velocity $\bar{V}_{\alpha_k}$ in Eq. (4) an amount

$$\Delta\bar{V}_{\alpha_k} = -\boldsymbol{n}_\alpha \cdot \boldsymbol{U}_{\beta_{nk}} e^{iK\theta_\alpha} \tag{12}$$

where $\boldsymbol{n}_\alpha$ is the normal to the driving rotor camber surface.

The calculation is performed using the iterative scheme described in Ref. 13, which amounts to a sequence of isolated rotor solutions [Eq. (4)] with intermediate velocity field calculations [from Eq. (6)]. Each isolated rotor solution is performed with the single rotation panel scheme described in Ref. 14.

Naturally, the number of harmonics retained and the number of iterations performed determines the overall computational cost. In the cases examined so far, it has been found that a single iteration is adequate to resolve the load-time histories with reasonable accuracy. Moreover, as will be demonstrated in the discussion of results, the Fourier series in Eq. (3) are rapidly convergent and typically 3-4 terms are retained in the final load evaluation. However, it is significant that the dominant contribution to the amplitude of each load

harmonic is from the uniteracted (steady) velocity field of the other rotor. Therefore the number of harmonics that must be interacted is smaller than the number that needs to be retained in the load evaluation. Typically only one or two harmonics are retained in the interaction. This point, which was not fully appreciated in Ref. 13, leads to significant reductions in computational cost.

Results

Results will be presented for cases in which the front and rear rotors are rigid and aligned with the axial flow so that the normal velocities V_F and V_R in Eq. (1) are steady($\omega_0 = 0$) and fixed by the advance ratio and geometric blade pitch. Also, in all the cases examined, $N_R = N_F$ and $\Omega_F = -\Omega_R = \Omega$. Therefore the blade loads are in phase ($m_0 = 0$), and the fundamental frequency is the blade passage frequency $2N\Omega$.

Two blade geometries have been studied, both low-speed straight blades. The HS3155 blade has aspect ratio 6 and a flat bottom CLARK-Y section with variable chord. This case was chosen because of the availability of counter-rotation performance data in Ref. 1. It has also been studied numerically by Lesieutre and Sullivan[4,5] and Chen and Williams.[6] The Purdue model blade has aspect ratio 3, constant chord, and NACA 0010 section. This case was chosen for comparison to Harrison's unsteady LDV velocity field measurements.[2,3] Single rotation comparisons for this rotor were presented in Ref. 13. References 1 and 3 contain details of the HS3155 and Purdue model blades, respectively.

Performance Characteristics

Mean performance results will be given here in terms of conventional propeller performance parameters: advance ratio J; thrust coefficient C_T; power coefficient C_P; and efficiency $\eta = JC_T/C_P$.

Figures 2 and 3 show mean performance results for a CRP system with two HS3155 blades per row with comparisons to Biermann's measurements. Combined system performance is shown in Fig. 3, and the power split between the two rotors is shown in Fig. 4. The calculation used two frequencies (0th and 1st harmonic of blade passage) in the normal velocity calculation and required only one iteration. The mean performance parameters depend only on the 0th harmonic of the blade loads.

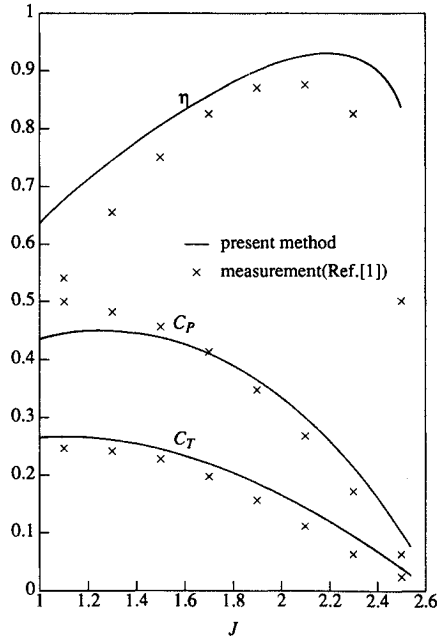

Fig. 2 CRP mean performance (2×2 HS3155, $\beta_F = 45$ deg, $\beta_R = 44$ deg, $x_{FR}/R = 0.16$).

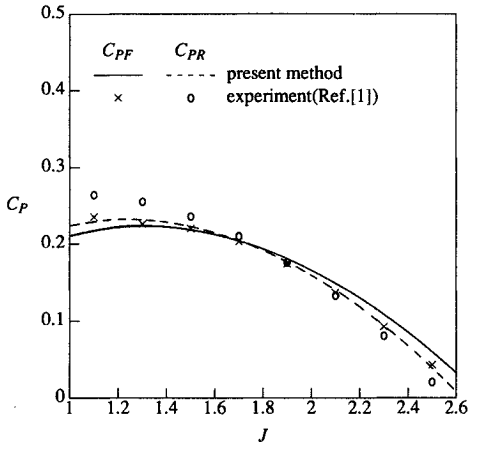

Fig. 3 Individual rotor power coefficient comparison (2×2 HS3155, $\beta_F = 45$ deg, $\beta_R = 44$ deg, $x_{FR}/R = 0.16$).

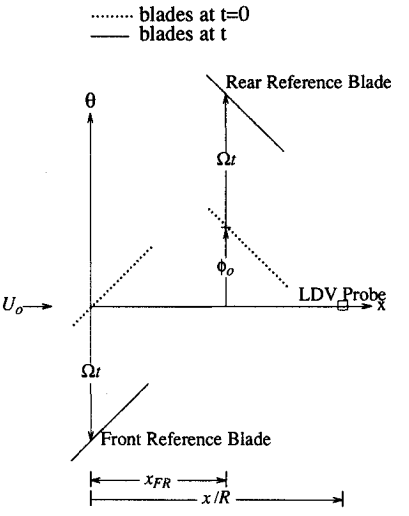

Fig. 4 Moving CRP system in θ-x plane.

The agreement is quite good except for the higher prediction of efficiency near windmill(bigger advance ratio) due to neglect of viscous drag and discrepancies at higher loading (smaller advance ratio), which are largely caused by the rigid wake model in the analysis. Note that the present method captures the power crossover near $J = 1.8$. Although it is not shown in this paper, basically the same qualitative agreement was found for a single rotation propeller (SRP) HS3155 blades.

Unsteady Loads

In this section, blade load fluctuations due to the unsteady interaction between rotors will be presented. Two configurations are examined: the 2 × 2 Purdue model and the 4 × 4 HS 3155.

The timing convention used is shown in Fig. 4. (The probe location indicated on the figure is relevant to the next section dealing with velocity field data.) Here we take the "initial phase" $\phi_0 = 0$ deg so that $t = 0$ means that the quarter-chord lines of the front and rear reference blades are aligned.

Since most of the computing time is consumed in the induced velocity calculation, it is important to keep the number of interacting harmonics to a minimum consistent with capturing the dominant unsteady characteristics of the loads. Figure 5 shows the effect of retaining higher harmonics on the unsteady section thrust at the 3/4 blade tip radius on the front and rear reference blades of the 2 × 2 Purdue model system. What is being varied is the number of harmonics velocity

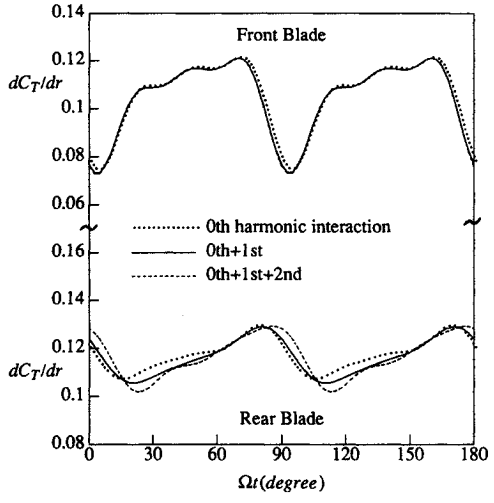

Fig. 5 Sectional thrust time history (2×2 Purdue model, $J = 1.78$, $\beta_F = \beta_R = 45.4$ deg, $x_{FR}/R = 0.35$).

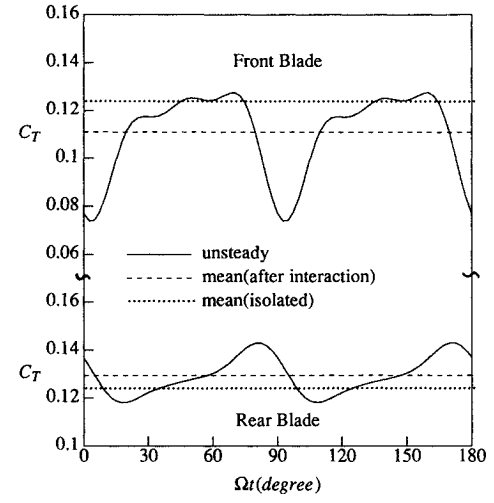

Fig. 7 Total thrust time history (2 × 2 Purdue M model, $J = 1.78$, $\beta_F = \beta_R = 45.4$ deg, $x_{FR}/R = 0.35$).

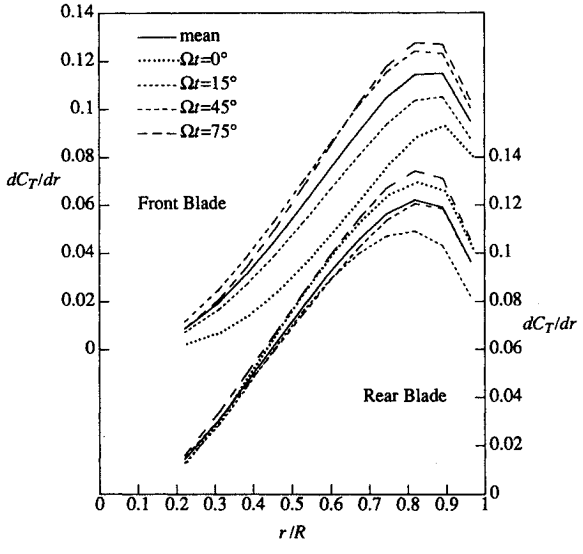

Fig. 6 Sectional thrust time history (2×2 Purdue model, $J = 1.78$, $\beta_F = \beta_R = 45.4$ deg, $x_{FR}/R = 0.35$).

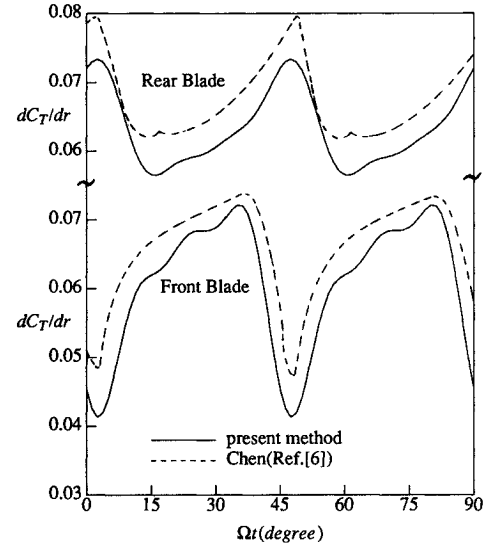

Fig. 8 Comparison of sectional thrust at $r/R = 0.75$ (4×4 HS3155, $J = 2$, $\beta_F = 45$ deg, $\beta_R = 44$ deg, $x_{FR}/R = 0.16$).

fields computed. The "0th harmonic interaction" result, e.g., is obtained if only the velocity field generated by the mean blade loads is computed. In the "0th + 1st" interaction, velocity fields for the first two load harmonics are included. It can be seen in the figures that the "0th harmonic interaction" captures the major part of the load fluctuation, especially on the front rotor. Including higher velocity harmonics adds little but computing cost. The wiggles seen in Fig. 5 are the result of representing a "saw tooth" shaped curve with four harmonics. (This saw tooth pattern can be easily deduced from a simple two-dimensional quasisteady point vortex model.) Increasing the number of load harmonics beyond four smoothes the wiggles but does not change the basic waveform or amplitude. All subsequent results in this paper were obtained with four load harmonics and two velocity harmonics (corresponding to the "0th + 1st" case in Fig. 5).

The magnitudes of the fluctuations in spanwise blade loadings are illustrated in Fig. 6 for the front and rear rotors, respectively. The amplitudes are comparable near the tip but differ substantially inboard. The front rotor has large fluctuations across the span, where the rear rotor has very small fluctuations inboard. It is likely that the bigger fluctuation on the front rotor is seen because its trailing edge passes near the highly loaded leading edge of rear rotor blade (while the rear rotor leading edge passes near the lightly loaded trailing edge of the front rotor). The large fluctuations at the tip of the rear blade are caused by interaction with the tip vortex of the front blade.

Figure 7 shows the unsteady total thrust on the front and rear rotors together with the mean values before and after interaction. We can see that after interaction the total thrust on the front rotor decreases while that on the rear rotor increases. In this particular case, the interaction decreases the total system thrust slightly.

Results for the 4×4 HS3155 CRP system were computed for direct comparison with Chen and Williams'[6] time-domain calculation. Figure 8 compares the sectional thrust at the 3/4 radius station. The unsteady fluctuations by both methods agree very well. The small discrepancies in mean thrust are mainly due to differing discretization errors and appear also in corresponding isolated rotor calculations with the two schemes.

The present scheme can be considerably cheaper than the time marching scheme. For the case of the 2×2 Purdue model system, the present method used as little a 1/10th of Chen and Williams' computing time (with 1 iteration using 1(0th) veloc-

ity harmonic and 4 load harmonics). At least part of the reason for this is that Chen and Williams paneled both the upper and lower blade surfaces and therefore used about twice as many panels per blade for the same load resolution as the lifting surface scheme. Moreover, Chen and Williams solve Eq. (1) simultaneously at each time step, rather than iteratively, so that his total influence coefficient matrix (using symmetry) is four times bigger (16 times more elements). This is partially offset by the necessity of computing velocity fields in the present scheme, which adds substantial CPU time (but little memory).

Most of the memory required by the present scheme is used to store the harmonic reference blade influence coefficient matrices for each rotor [$\bar{A}_{\gamma\gamma}$ in Eq. (4)]. If 4 load harmonics are retained, this amounts to 8 complex valued matrices, each $N_p \times N_p$ (where N_p is the number of panels on the reference blade). With 100 panels on the blade, this is equivalent to $8 \times 2 \times 100 \times 100 = 1.6 \times 10^5$ floating point numbers. Of course the memory requirements can be traded off with CPU time by recomputing the matrices as needed.

Induced Velocities

Once the loads on the front and rear rotors have been determined, the velocity induced by those loads can be computed at any point using Eq. (6). This has been done for the 2×2 Purdue model CPR system for which extensive experimental data are available.

The induced velocity fields at one downstream plane ($x/R = 0.683$) and at one plane between the front and rear rotors ($x/R = 0.22$ 5) were computed at 14 radial stations from $r/R = 022$ to $r/R = 1.1$ in 3-deg increments circumferentially covering a half circle. The results will be compared in this section to corresponding LDV measurements made by Harrison.[2,3] (Similar computational/experimental comparisons for single rotation were presented in Ref. 13.)

A broad picture of the computed flowfield can be seen in the crossflow vector plots in Figs. 9 and 10. These pictures illustrate the entire instantaneous crossflow fields at each axial station. The axial velocity is directed into the plane. The front rotor (reference blade location is labeled B_F) rotates clockwise, and the rear rotor (labeled B_R) rotates counterclockwise. The tip vortices shed from the front and rear reference blades are labeled V_F and V_R, respectively. The reader should distinguish the instantaneous phase angle between the rotors (ϕ in Fig. 1) from the initial phase angle between the rotors at $t = 0$ (ϕ_0 in Fig. 4). At $\phi = 0$ deg, the two reference blades are aligned along the positive y-axis of Fig. 1.

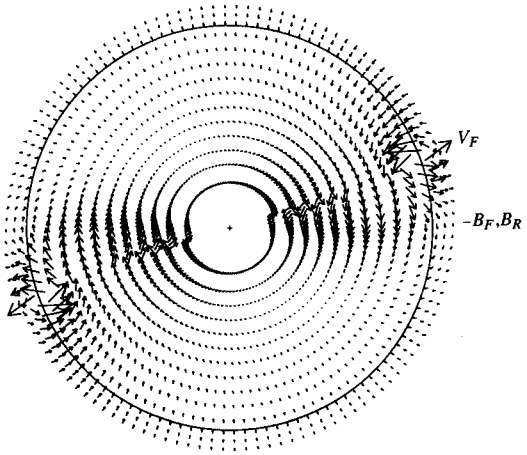

Fig. 9 Instantaneous crossflow at $x/R = 0.225$ (between the rotors), $\phi = 0$ deg (2×2 Purdue model, $J = 1.78$, $\beta_F = \beta_R = 45.5$ deg, $x_{FR}/R = 0.35$).

Between the rotors, Fig. 9, the two tip vortices and vortex sheet shed from the forward rotor are evident. Only one phase ($\phi = 0$ deg) is shown, but to a large extent this field simply rotates with the front blades and is similar to the single rotation results of Ref. 13. At the downstream station, three phase angles ($\phi = 0$, 60, and 120 deg) are shown in Figs. 10a–10c. Here, of course, we see the tip vortices and wakes from all four blades. The front and rear tip vortices cross between 60

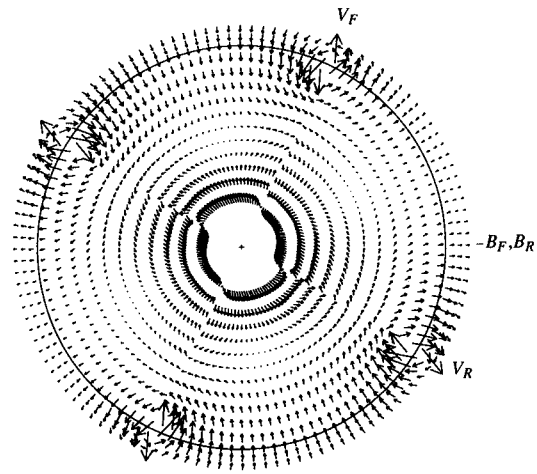

a) $\phi = 0$ deg (2×2 Purdue model, $J = 1.78$, $\beta_F = \beta_R = 45.5$ deg, $x_{FR}/R = 0.35$)

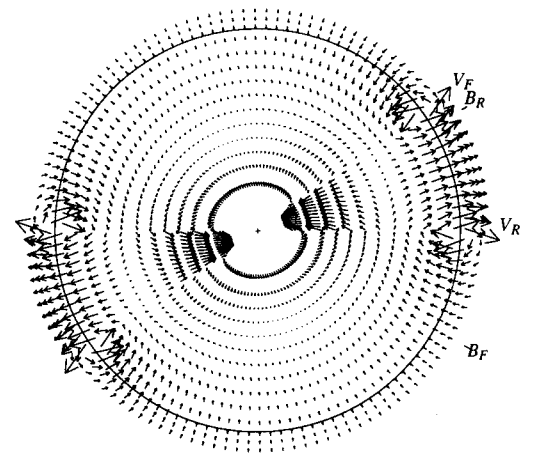

b) $\phi = 60$ deg

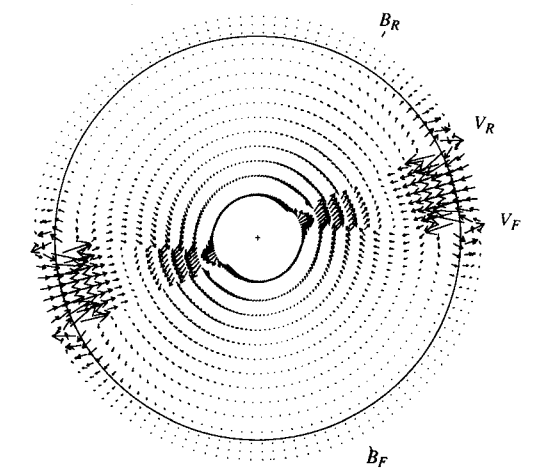

c) $\phi = 120$ deg

Fig. 10 Instantaneous crossflow at $x/R = 0.683$ (downstream).

and 120 deg producing strong radial jets. To some extent, which will be quantified later, this downstream flow can be treated as the superposition of the noninteracted flows from the front and rear rotors in isolation.

Harrison's data set is not large enough to construct instantaneous crossflow plots (e.g., Fig. 9). Therefore the comparisons have been made in terms of time histories, in Figs. 11–14. This has been done in two ways. Figures 11 and 13 are time histories of velocity components at three radii each. Radial distributions of the crossflow are given in Figs. 12 and 14. Note that the circumferential position in these plots indicates time (Ωt) *not* spatial positions so that the complete circle covers two blade passage periods. Computational results are given in one passage period, and experimental results in the other. Figures 11 and 12 are for the plane between the rotors with 0 deg initial phase. The remaining figures are for the downstream plane at a phase angle $\phi_0 = 120$ deg (see Figs. 13 and 14).

The multiplicity (or scatter) of the measured data can be explained as follows. Velocity components were measured in two scans, each covering one complete rotation or two passage periods. The "horizontal" scan provided axial (U_x) and tangential (U_θ) velocity components. The "vertical" scan provided axial (U_x) and radial (U_r) components. Therefore we plot four axial, two tangential, and two radial components in one passage period. The scatter in tangential and radial components results mainly from small blade "mistuning." The scatter in axial velocity results from that and tunnel effects (since the probe positions are different in the horizontal and vertical scans) as well as measurement errors caused by probe orientation with respect to the flow direction.

Two computational results are shown in Figs. 11 and 13. The "uninteracted" results are obtained by simple superposition of SRP calculations (discussed in Ref. 13). The solid lines are computed with interaction. Although the unsteady calculation shows slightly better agreement with the measured data, it is apparent that major features of the velocity field are captured quite well by superposition of the isolated rotor fields.

Most of the obvious differences between the calculated and measured flows can be explained in terms of the rigid wake model used in the calculation. The measured data show a thin viscous wake (e.g., near 15 deg in Fig. 11a), which is of course missing in the calculation. More significantly, the tip vortices suffer some axial and radial contraction, which shows up as phase and amplitude errors in the calculation. For example, in Fig. 11c the disturbance near 170 deg is caused by the upstream influence of the rear blade and is captured with little phase error by the calculation. However, the disturbance near 15 deg is caused by the tip vortex from the front blade, and measured velocity peaks lead the calculated ones by around 5 deg. The most dramatic effect of this type is seen in Fig. 13b, which, with $r/R = 0.97$, is just inboard of the uncontracted tip vortices. The first velocity peak is generated by the rear rotor tip vortex, the second by the front vortex. Contraction of the front blade vortex is large enough that this radius is actually outboard from the vortex core, not inboard so that the pre-

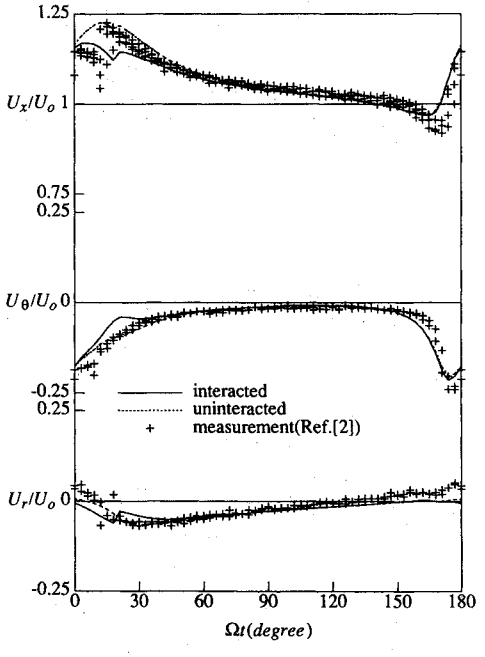

a) $r/R = 0.75$ (2×2 Purdue model, $J = 1.78$, $\beta_F = \beta_R = 45$ deg, $x_{FR}/R = 0.35$)

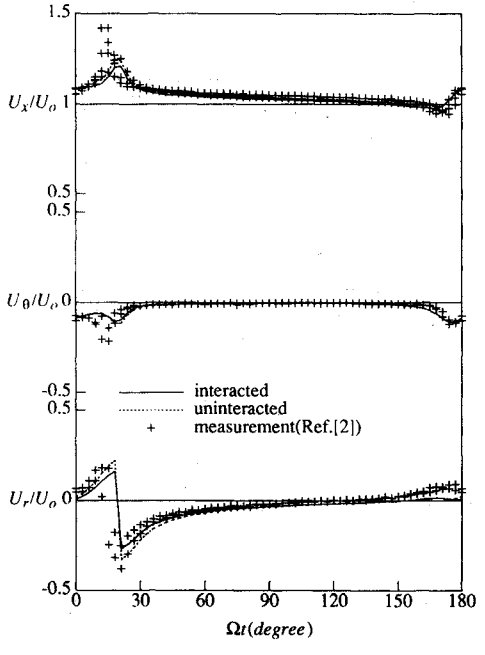

b) $r/R = 0.97$

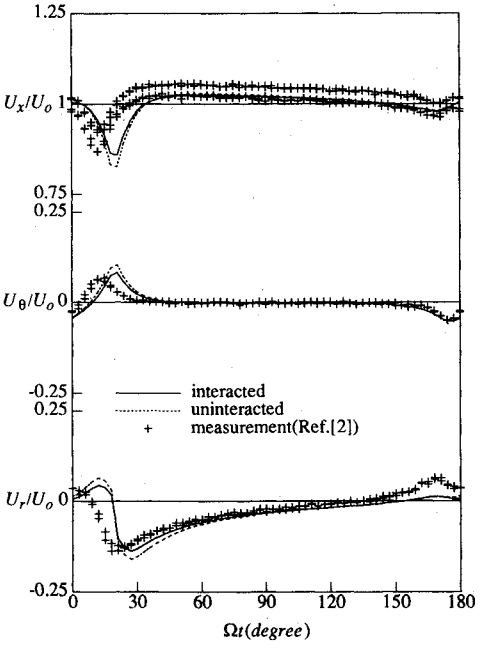

c) $r/R = 1.06$

Fig. 11 Velocity time history at $x/R = 0.225$, $\phi_0 = 0$ deg.

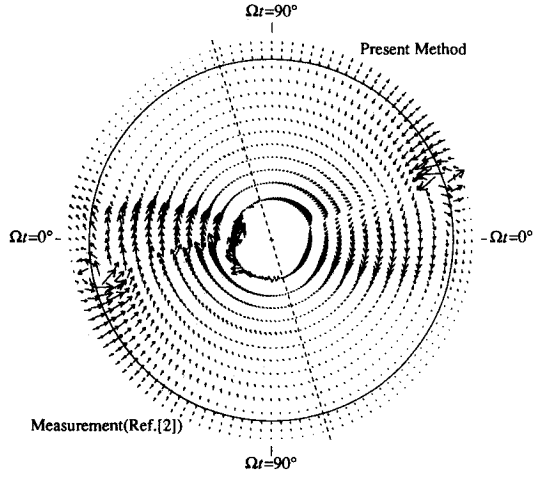

Fig. 12 Crossflow time histories at $x/R = 0.225$, $\phi_0 = 0$ deg (2×2 Purdue model, $J = 1.78$, $\beta_F = \beta_R = 45.5$ deg, $x_{FR}/R = 0.35$).

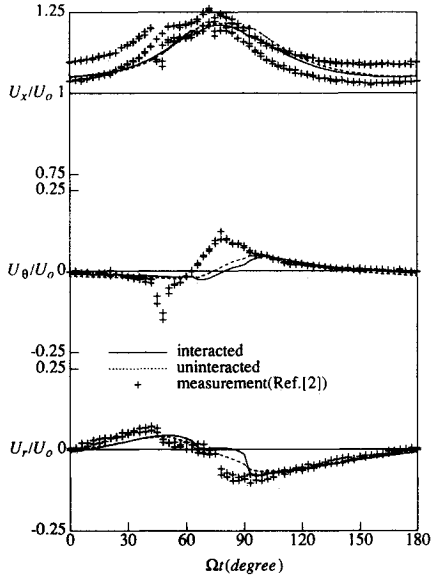

a) $r/R = 0.75$ (2×2 Purdue model, $J = 1.78$, $\beta_F = \beta_R = 45.4$ deg, $x_{FR}/R = 0.35$)

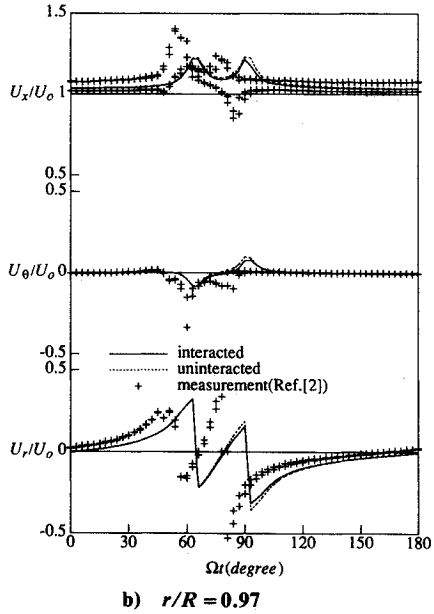

b) $r/R = 0.97$

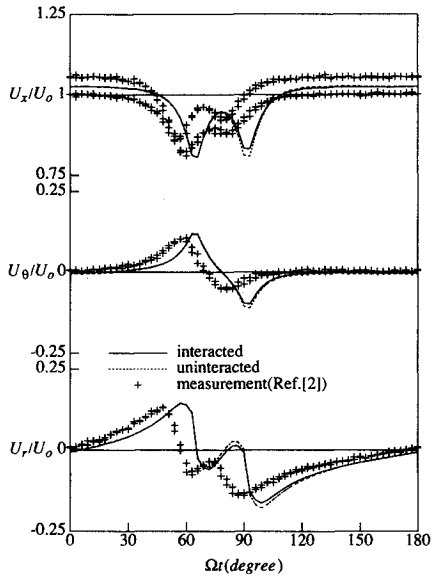

c) $r/R = 1.06$

Fig. 13 Velocity time history at $x/R = 0.683$, $\phi_0 = 120$ deg.

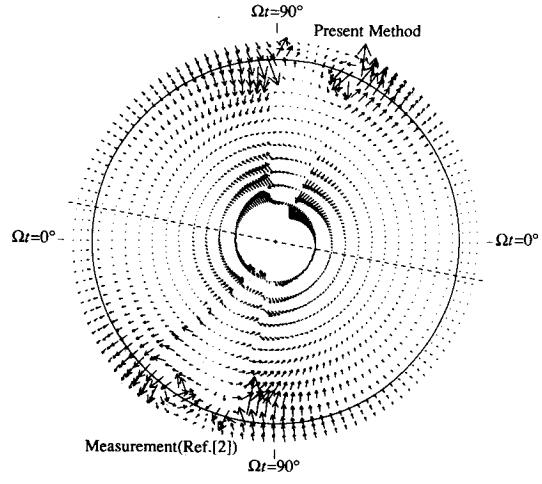

Fig. 14 Crossflow time histories at $x/R = 0.683$, $\phi_0 = 120$ deg (2×2 Purdue model, $J = 1.78$, $\beta_F = \beta_R = 45.4$ deg, $x_{FR}/R = 0.35$).

dicted second axial velocity peak goes the wrong way. Further outboard at $r/R = 1.06$ (see Fig. 13c), this contraction simply produces smaller measured peak velocities than predicted. Again the phase errors in the results are caused by axial contraction, as seen between the blade rows.

The details of the flow near the blade tip radius is of course very sensitive to small displacements of the measurement point since the velocities vary rapidly near the tip vortices. Large local errors in prediction, therefore, can and do occur. However, it is evident from Figs. 12 and 14 that the overall flow pattern predicted by the model does closely mimic the measurements.

Conclusions

The multiple harmonic, frequency-domain panel method presented here has been applied to the prediction of mean and fluctuating loads and the induced velocity field of a counter-rotating propeller. The mean load and velocity field results have been verified by comparison to experimental data. The fluctuating loads have been shown to agree with those predicted by an independent time marching algorithm, but at substantially less computational cost.

The results suggest that useful mean performance predictions can be made with a simplified model wherein the circumferentially averaged (isolated) propwash generated by the other rotor is imposed on each to correct for mutual interference. All other (higher harmonic) interaction terms appear to have negligible effect on the mean performance.

It was also found, at least for the cases examined, that the blade load fluctuations could be evaluated with reasonable accuracy by ignoring the velocity fields generated by all blade harmonics other than the first (i.e., mean). Higher harmonics do need to be retained in the load evaluation.

These properties are clearly related to the observation that the unsteady velocity field about the CRP system could be represented quite well by simply adding together the (individual steady) velocities of the isolated rotors. To what extent these conclusions may hold at smaller rotor separation or higher prop loading than have been examined is unclear. The underlying panel method has clear high power limitations even for isolated rotors. Inclusion of some type of free-wake model would undoubtedly improve the predictions, particularly at high power.

The panel method also can give poor results at very large frequencies (when the wavelength becomes comparable to the panel size). This was a problem in the wing-propeller interaction analysis of Ref. 13 because of large wing chord. It could be a problem for CRP analysis when the number of blades is large and/or the advance ratio is low.

Since the present scheme computes the fluctuating blade loads, it can clearly be used for forced vibration analysis of counter-rotating systems. The method (including elastic blade modes) has been extensively used for forced response and flutter analysis of single rotation propellers. Similar application to CRP systems now appears feasible.

Acknowledgment

The work reported here has been partially supported by NASA Lewis Research Center under Grant 3-499.

References

[1]Biermann, D., and Hartman, E. P., "Wind-Tunnel Tests of Four- and Six-Blade Single- and Dual-Rotating Tractor Propellers," NACA Rept. 747, 1942.

[2]Harrison, G. L., and Sullivan, J. P., "Measurement of a Counter Rotation Propeller Flowfield Using a Laser Doppler Velocimeter," AIAA Paper 87-0008, Jan. 1987.

[3]Harrison, G. L., "An Experimental Investigation of the Flow Field around a Counter-Rotating Propeller System Using a Laser Doppler Velocimeter," Ph.D. Thesis, Purdue Univ., West Lafayette, IN, 1987.

[4]Lesieutre, D. J., and Sullivan, J. P., "The Analysis of Counter-Rotating Propeller Systems," Society of Automotive Engineers, Warrendale, PA, SAE Paper 8500869, April 1985.

[5]Lesieutre, D. J., and Sullivan, J. P., "Unsteady Forces on Counter-Rotating Propeller Blades," AIAA Paper 86-1804, June 1986.

[6]Chen, S. H., and Williams, M. H., "A Panel Method for Counter Rotating Propfans," AIAA Paper 87-1890, July 1987.

[7]Williams, M. H., "An Unsteady Lifting Surface Theory for Single Rotation Propellers," Purdue Univ., West Lafayette, IN, Purdue Univ. Rept., June 1985.

[8]Williams, M. H., "User's Guide to UPROP3S," Purdue Univ., West Lafayette, IN, Purdue Univ. Rept., Jan. 1985.

[9]Williams, M. H., and Hwang, C., "Three Dimensional Unsteady Aerodynamics and Aeroelastic Response of Advanced Turboprops," AIAA Paper 86-0846, May 1986.

[10]Kaza, K. R. V., Mehmed, O., Narayanan, G. V., and Murthy, D. V., "Analytical Flutter Investigation of a Composite Propfan Model," AIAA Paper 87-0738, April 1987; also NASA TM-88944.

[11]Kaza, K. R. V., Mehmed, O., Williams, M. H., and Moss, L., "Analytical and Experimental Investigation of Mistuning in Propfan Flutter," AIAA Paper 87-0739, April 1987; also NASA TM-88959.

[12]Williams, M. H., "Aeroelastic Effects of Alternating Blade Sweep on Advanced Propfan Rotor," American Society of Mechanical Engineers, New York, ASME Paper 87-WA/AERO-8, Dec. 1987.

[13]Cho, J., and Williams, M. H., "Propeller-Wing Interaction using a Frequency Domain Panel Method," *Journal of Aircraft*, Vol. 27, No. 3, March 1990, pp. 196–203.

[14]Cho, J., "Frequency Domain Aerodynamic Analysis of Interacting Rotating Systems," Ph.D. Thesis, Purdue Univ., West Lafayette, IN, 1988.